EPOXI Calibration Pipeline Summary

Last Revised May 11, 2014

1.0 Calibration Pipeline Processing

This report summarizes the pipeline used to calibrate these data currently in the NASA Planetary Data System (PDS):

- Version 1.0 EPOXI HRI-VIS and MRI-VIS Hartley 2 images (McLaughlin, et al., 2012b; McLaughlin, et al., 2012c),
- Version 2.0 EPOXI HRI-IR Hartley 2 spectra (McLaughlin, et al., 2013a),
- Version 2.0 EPOXI/EPOCh HRI-VIS and MRI-VIS Earth and Mars images (McLaughlin, et al., 2012d; McLaughlin, et al., 2012e; McLaughlin, et al., 2012f; McLaughlin, et al., 2012g), and
- EPOXI/EPOCh HRI-IR Earth Version 2.0 and Mars Version 1.0 spectra (McLaughlin, et al., 2014g; McLaughlin, et al., 2014h),
- Version 1.0 EPOXI HRI-IR comet Garradd spectra (McLaughlin, et al., 2014i)
- Version 1.0 EPOXI HRI-VIS and MRI-VIS comet Garradd images (McLaughlin, et al., 2014j; McLaughlin, et al., 2014k)
- Version 1.0 EPOXI HRI-IR comet ISON spectra (McLaughlin, et al., 2014l)
- Version 1.0 EPOXI MRI-VIS comet ISON images (McLaughlin, et al., 2014m)
- Version 3.0 EPOXI HRI-IR Hartley 2 spectra (McLaughlin, et al., 2014a),
- Version 1.0 EPOXI HRI-IR Lunar Calibrations spectra (McLaughlin, et al., 2014b),
- Version 3.0 Deep Impact HRI-IR Tempel 1 spectra (McLaughlin, et al., 2014c)
- Version 3.0 Deep Impact HRIV, MRI, and ITS Tempel 1 images (McLaughlin, et al., 2014d; McLaughlin, et al., 2014e, McLaughlin, et al., 2014f).

For more details about the calibration pipeline and its processes, see *EPOXI Instrument Calibration* by Klaasen, et al. (2013) and *Deep Impact Instrument Calibration* by Klaasen, et al. (2008).

1.1 Standard Steps

The EPOXI pipeline applies a standard set of procedures and settings to each VIS or IR image in order to automatically calibrate all data (see Figure PIPELINE). In general, these default settings are the best the science team was able to derive for the dataset as a whole and thus do not necessarily reflect the best possible processing for any particular image. For special cases, the automated pipeline has the ability to specify special settings for particular observations.

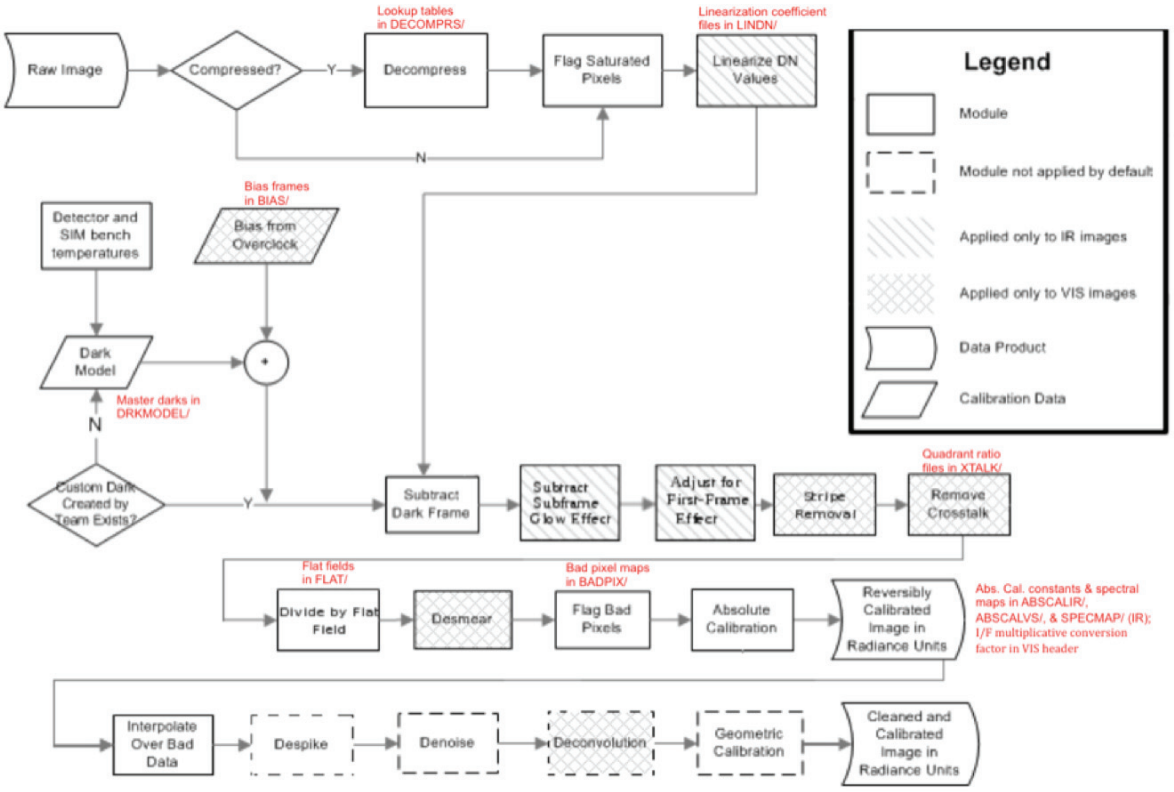

Figure PIPELINE – Logic flow for the EPOXI calibration pipeline as described in *EPOXI Instrument Calibration* by Klaasen, et al. (2013). Some modules are not applied to all instruments. The Despike, Denoise, Deconvolution, and Geometric Calibration modules were turned off for all data. Input calibration files and their location in the CALIB/ subdirectory within a PDS dataset are identified by red text. The pipeline is based on the one used for the Deep Impact prime mission as discussed in *Deep Impact Instrument Calibration* by Klaasen, et al. (2008).

The standard pipeline begins by decompressing the image if it was compressed on the spacecraft. Images can be compressed using one of four 14-bit to 8-bit lookup tables optimized for different types of exposures. To uncompress the images, a reverse lookup table is used which maps each 8-bit value to the average of all corresponding 14-bit values.

All saturated and missing pixels are flagged in the quality map. Then an IR image is linearized using the derived correction function. Linearization is the first step for IR data because the IR output data represent a read-minus-reset DN value causing all output DN values to represent signal collected in the detector (any fixed bias is subtracted out) and to be subject to the non-linearity of its response. A VIS image does not need this step because the instrument responds linearly.

Next, a dark frame is subtracted from the image. If a dark frame has been created by the science team for the specific observation, then it is subtracted. Otherwise, a dark model is used to generate the frame (for a thorough discussion of dark pattern removal, please see *EPOXI Instrument Calibration* by Klaasen, et al., 2013).

After the dark subtraction, a VIS image undergoes a few extra processing steps not taken by every IR image. First, residual stripes extending along the rows of each image quadrant are

examined. If they can be accurately measured, they are removed from the image and stored as an image extension. Then, the electrical crosstalk is removed by subtracting a derived ghost frame. Each quadrant in this frame is a linear combination of rotated versions of the other three quadrants. Next, the image (both VIS and IR) is divided by a flat field in order to account for variable responsivity across the detector. Lastly, VIS CCD transfer smear is removed using the parallel overclock rows if the image was taken in modes one through six or a column averaging approximation if the image is in modes seven or eight (for more detail about transfer smear, see *EPOXI Instrument Calibration* by Klaasen, et al., 2013).

After bad pixels are flagged, the image is radiometrically calibrated to produce a radiance image in W/[m^2 sr μm]. For a VIS image, this is simply done by dividing the image by integration time and then multiplying by the appropriate conversion factor for the given filter and desired output. Once the VIS radiance image is created, the pipeline computes a multiplicative factor (pi divided by the solar spectrum at the target's distance from the sun) to convert from radiance to I/F and stores the factor in the VIS header. For an IR image, the procedure is more complicated as the absolute calibration is wavelength dependent, which in turn is temperature dependent. First, the wavelength and bandwidth for each pixel are calculated. Then, each pixel is multiplied by the appropriate wavelength-dependent calibration factor and divided by the pixel's integration time and spectral bandwidth.

At this point, a reversible radiance image data product has been created, and a copy is run through the rest of the pipeline, which performs a series of non-reversible steps. First, the data are interpolated over the bad pixels and gaps. For a VIS image, this interpolation is performed using thin plate splines anchored by the valid data around the edges of each hole. For an IR image, a linear interpolation is performed in the spatial dimension only. Next for a VIS image, the pixel values in the overscan rows and columns that border the active area of the CCD are not preserved as in RADREV but are overwritten with 0.

Next, an optional despiking routine is applied in order to remove cosmic rays. This routine performs a sigma filter by calculating the median of each NxN box, where N is odd, and then replacing the central pixel with the median if it is more than M median deviations from the median. By default, both M and N are set to 3. The median deviation of a set S is defined as: $Med(|\, S - Med(S)\,|)$.

Lastly, a VIS image may be deconvolved using the derived point-spread function of the instrument. This optional step is especially important for the HRI-VIS instrument, which is out of focus.

1.2 Calibration Quality Map

Along with each calibrated image, a byte map is created that defines the data integrity for every pixel. For each byte in the map, representing one pixel, each bit acts as a flag that is set to 1 if the given criterion is met for that pixel. These flags are:

MSB							LSB
7	6	5	4	3	2	1	0

0. Bad Pixel - This pixel is a known bad pixel.
1. Missing - The datum for this pixel was not received from the spacecraft.
2. Despiked - This pixel was modified by the despiking routine.
3. Interpolated - This pixel has been reclaimed by interpolating from its neighbors.
4. Some Saturated - The raw value for this pixel is above the point where some pixels become saturated. For VIS instruments, this occurs at 11,000 DN, while for the IR spectrometer, this occurs at 8,000 DN.
5. Most Saturated - This raw value for this pixel is above the point where most pixels are full-well saturated. For VIS instruments, this occurs at 15,000 DN, while for the IR spectrometer, this occurs at 11,000 DN.
6. ADC Saturation - The ADC was saturated for this pixel.
7. Ultra Compressed - The pixel was in a compression bin so large that the value contains very little information.

For example, if the pixel is bad and has been reclaimed by interpolation, the decimal value in the quality map will be $2^0 + 2^3 = 9$. In the normal FITS format for the calibrated image, this map exists as the first image extension.

1.3 Signal-to-Noise Ratio Map

In order to provide more information to the end user, another image extension is created to provide the estimated signal-to-noise ratio (SNR) for each pixel. The signal is taken to be the dark- and bias-subtracted image value in 14-bit DN, while the noise estimate consists of the root-sum-squared of three different noise sources: shot noise, read noise and quantization noise. The shot noise in 14-bit DN is defined as:

$$N_s = \sqrt{\frac{Raw - Bias}{K}}$$

where K is the gain in electrons/14-bit DN and is dependent on the instrument and mode, and *Raw* and *Bias* are in 14-bit DN. For the IR spectrometer, *Bias* is 0 by definition except in Mode 6. The quantization noise is defined as:

$$N_q = \frac{Q}{\sqrt{12}}$$

where Q is the quantization step in 14-bit DN (N_q represents the rms error introduced by quantizing a signal whose true value could lie anywhere within the quantization bin with equal probability, i.e.,

$$\sqrt{\frac{\int_{-\Delta/2}^{\Delta/2} \in^2 d \in}{\Delta}}$$

where Δ = the quantization step size and $\in$ = the quantization error). For uncompressed data, Q depends on the performance of the ADC, while for compressed data, Q is set to the bin size in

the decompression lookup table that the pixel used or to the uncompressed Q value, whichever is larger. The parameter values needed for the noise calculation were determined from instrument calibrations and are shown in Table 1.

Instrument	K (e/DN_{14})	Uncompressed Q (DN_{14})	Read Noise (DN_{14})
IR Unbinned	16	1	5.0
IR Binned	64	1	3.0
HRI	27.4	2	0.7
MRI	27.2	2	1.0
ITS	30.5	2	1.2

Table 1 - Noise parameters determined in calibrations of all instruments (Klaaset, et al., 2008).

1.4 Spectral Registration Maps

In an IR image product, two additional image extensions are included: one provides the effective wavelength (spectral registration) of each pixel and another provides the spectral bandwidth for each pixel.

1.5 Optional Steps

Beyond the automated calibration pipeline described here, a manual calibration can be performed where the user can specify his/her own settings and calibration files for each step. Also, any processing module can be disabled, and there are two extra ones that can be enabled. The first such module is a noise-reduction module that is applied after the despiking routine. This module applies the BayesShrink wavelet thresholding algorithm with a robust mean noise estimator to remove some of the noise. The other step that can be enabled applies a rubber sheet geometric distortion correction. This function is not normally applied, as the optical distortion though the telescope is minimal.

2. Pipeline Updates

The updates to the instrument calibrations derived during EPOXI required changes to the data processing pipeline software as it existed at the end of the DI mission. In addition, science team internal reviews and peer review of previous DI data slated for archive brought to light some errors in the existing calibration code that were corrected.

2.1 New files and constants

The simplest pipeline updates involved adding updated, or removing obsolete, calibration files and calibration constants that track the time-varying performance of the instruments. These were added to the database of previous calibration files along with the applicable time periods for each, and no software changes were usually required for the pipeline to be able to use these files. In addition, the new calibration files, stored in FITS format, were given enhanced labels with comments describing provenance, pixel orientation, and how each file is meant to be used in DI data calibrations. These files are documented in the PDS archive of the calibration, and are

summarized here by the first date (YYMMDD: YY=year; MM=month; DD=day of month) of data affected by each set of files:

050112	Revised all MRI-VIS calibration constants
050112	Updated IR flat fields that include the Anti-Saturation Filter and removed previous IR flat field place holders from calibration database
050112	Updated IR spectral smile equation
050112	Updated IR absolute calibration based on Vega and Beta Hyi observations, including 2x correction
071001	Updated IR flat fields that include the Anti-Saturation Filter using pixel-by-pixel processing and removed previous IR flat fields from calibration database
071001	Updated IR quad-averaged linearization coefficients
071001	Updated IR master dark file
071001	Updated IR absolute calibration based on Beta Hyi and Vega observations obtained from 2009 to 2011
071004	Updated IR bad pixel maps from 01/2008 calibration
071004	Updated IR read noise values from 2008 calibration
071004	Updated HRI-VIS 950-nm filter calibration constant from 2008 calibrations
071004	Updated VIS cross-talk files from 2008 and 2010 calibrations
080528	Updated IR bad pixel maps from 06/2008 calibration
080623	Updated IR quad-averaged linearization coefficients
090601	Updated IR bad pixel maps from 06/2009 calibration
090618	Updated IR quad-averaged linearization coefficients
100101	Updated HRI-VIS 950-nm filter calibration constant from 2010 calibrations
100101	Updated all MRI-VIS filter calibration constants by 5%
100201	Updated VIS flat fields
100201	Updated IR bad pixel maps from 02/2010 calibration
100216	Updated quad-averaged IR linearization coefficients
100801	Updated IR read noise values from 09/2010 calibration
100901	Updated all HRI-VIS filter calibration constants (except 950-nm) by 3%
100928	Updated IR bad pixel maps from 02/2011 calibration using pixel-by-pixel linearity constants from 02/2011
100928	Updated IR linearization coefficients using a pixel-by-pixel technique from 02/2011 calibration
100928	Updated IR master dark files for each mode using pixel-by-pixel processing and calibration data from 02/2011

2.2 Compressed 0-DN fix

Because of the issue in decompressing 0 DN compressed VIS data (Sec. 5.3.6 in Klaasen, et al., 2013), the pipeline software was changed to decompress the VIS cameras' zero LUT entry, and only that entry, to the top of its range, i.e., to 350 DN. Also, because it could not be ascertained whether the original pixel's 14-bit DN value was actually 350 or a lower value, all such pixels were marked as SATURATED in the FLAGS FITS extension, the rationale being that just as the actual value of a saturated pixel at the upper end of the possible DN range (255 for compressed 8-bit DNs; 16383 for uncompressed 14-bit DNs) cannot be determined, the same is true for a

pixel at the lower end of the range. The user of the FITS file can easily determine the type of saturation of such a flagged pixel by examining its stored value.

2.3 IR transient background correction

A mathematical model for the transient behavior of the IR background signal has been implemented based on the effects of charge trapping (Sec. 4.3.3 in Klaasen, et al., 2013). Calibrating the IR background transients requires knowledge of the detector reset and read history. To minimize this effect for Hartley 2 encounter data, four IR frames were taken immediately before, and with the same mode and integration time as, each downlinked data sequence. However, these four-frame sets were never saved and downlinked. As such, the frame header information on the ground is incomplete for making the background transient correction. Therefore, planning data from sequencing spreadsheets are parsed by the pipeline software and used to reconstruct IR detector reset/read history and perform the background transient calibration. The data critical to this analysis will be extracted from the sequencing spreadsheets and archived with the relevant PDS data sets along with an explanation of how to use them. This correction is not applied in the standard pipeline processing but is available as a separate user option.

2.4 VIS stripes removal

Several techniques were developed by the Science Team to deal with residual observation-dependent, semi-coherent stripes on the order of 1 DN in the VIS background data (Sec. 5.3.3 in Klaasen, et al., 2013). Calibration procedures to deal with these effects (Sec. 5.3.3 in Klaasen, et al., 2013) were added to the pipeline software, though not always run in the pipeline by default. An additional extension that saves the stripe-removal adjustments for each line of each quad was added to retain the reversibility of the calibration. This extension records the de-stripe correction as a 2xN pixel array, where N is the number of rows in the primary image (e.g., 1024 or 512). The extension has units of DN. The first column of this de-stripe extension is the one-dimensional array of corrections subtracted from image columns <=M, where M is the middle column of the primary image (i.e., 512 for a 1024 column image, 1-based indexing). The second column of this de-stripe extension was subtracted from image columns numbered >M. Note that the serial overclock columns that border the primary image array are not modified by the de-stripe procedure. If the de-stripe correction was not applied, then all values in this extension are set to 0.

For a bright source such as Earth, scattered light can reach the edge of the image, and stripe removal considers it as a broad stripe and attempts to remove it. (The scattered light appears to be the normal fall off in surface brightness due to the bright source.) Although this correction does not adversely affect the data, technically the stripe removal routine should only remove stripes and not any scattered light. To reconstruct the full frame stripes image from the stripe extension: make a full frame of the two columns of stripe DN values, divide by the flat, divide by the integration time in seconds, and multiply by the radiance calibration constant. The image of stripes will now be in units of W/m^2/steradian/micron, and can be added to the RADREV or RAD image to undo the destriping (that is, to ‘restripe’ an image).

2.5 IR flat-field update

Improved lunar calibration data acquired during EPOXI allowed construction of an IR Spectrometer flat-field calibration file (Sec. 4.3.7 in Klaasen, et al., 2013). The new flat-field correction algorithm includes the correction for the Anti-Saturation Filter (ASF) in the flat-field calibration step. In prime DI mission calibrations, on the other hand, the flat-field correction ignored the change across the ASF boundary, and the correction for the ASF was implemented using two different absolute calibration curves, one of which was applied outside the ASF and the other inside the ASF.

2.6 IR ALTFF line-dependent integration time

Ongoing analysis of IR timing (Sec. 4.3.3 in Klaasen, et al., 2013) revealed that read and reset timings differ in the ALTFF mode, and the effective exposure time varies with line number, i.e., along the slit in the spatial direction. This variation has been modeled in the pipeline software, and line-specific integration times are used to convert from DN to DN/s in the ALTFF mode.

2.7 VIS flat-field file re-orientation

Pipeline code was modified to change the orientation of pixels in the flat-field calibration file, including POCs and columns and rows just inside OCs, to match that in the flight images. Earlier calibration files interleaved pixels by quadrant and shifted the overclocked pixels to the end of the rows and columns of each quadrant, which is how calibration images were generated from pre-launch ground calibrations. A keyword in the FITS header designates the pixel orientation.

2.8 Transposed VIS cross-talk corrections

During ingestion of the most recent data into PDS-SBN, we discovered that a new method to apply the cross-talk correction transposed the coefficients within the cross-talk xshift correction matrices used for cross-talk correction of the MRI- and HRI-VIS images. This happened when the new method was introduced into the calibration pipeline in January 2009 and affected the calibration of all data with observation dates of 2007-10-04 and later.

The cross-talk corrections are generally significant only when some parts of the images are near saturation, so for the vast majority of calibrated images the error introduced by the incorrect VIS cross-talk corrections can be safely ignored. Therefore we decided not to re-run the calibration pipeline on all images.

If a significant error may have been introduced into a specific MRI- or HRI-VIS image due to incorrect VIS cross-talk corrections, an examination of the FITS header of the calibrated image can permit identification of the calibration files used. If the name of the calibration file, as listed in the calibrated image FITS header keyword XTALKFN, has 071004_1 or 071004_2 or 071004_3 in it, then the coefficients in the crosstalk xshift correction matrix were transposed for the cross-talk correction, resulting in an image in which the crosstalk has not been appropriately corrected. Fixing the calibrated image requires removal of the incorrect crosstalk correction and replacing it with the correct crosstalk correction.

2.9 Header fixes and elimination of I/F files

The pipeline software changes described above generated changes in the calibrated data FITS headers, such as: whether or not a calibration step was applied; calibration files used; constants used; other parameters; and previous observation history. Where appropriate, new calibration steps are included in the SNR extension.

Also, since the VIS reflectance (I/F) calibrated data differ from the radiance data by only a constant factor, the pipeline no longer generates I/F files. It instead generates only the radiance data file and includes the conversion factor from radiance to I/F in the FITS header. For the IR spectrometer, the I/F version was judged not useful due to the presence of thermal emission from the source.

2.10 PDS Version 2

2.10.1 Hartley2 IR Spectrometer Data

Version 1 of the HRI-IR Hartley 2 data archived with the PDS (McLaughlin, et al., 2011), does not include the pixel-by-pixel (i.e., per-pixel) linearity correction treatment and its propagation through the calibration steps (i.e., bad-pixel map, flat-field file update, revised spectral calibration curve), the mode-dependent master darks, nor the optimized scaling factor for the master dark. Since Version 1, a refinement in the absolute spectral calibration curve was implemented, the sub-frame master darks were improved to now include the effect of glow from saturated border pixels (Sec. 4.3.3 in Klaasen, et al., 2013), and non-image pixels at the right, left and bottom edges of calibrated RADREV and RAD spectral images have been set to zero. These improvements are all included in Version 2 archived in the PDS (McLaughlin, et al., 2013a).

2.10.2 EPOCh Earth and Mars IR Spectrometer Data

Version 1 of the HRI-IR Earth EPOCh data archived with the PDS (McLaughlin, et al., 2009a) does not include the factor of 2 adjustment for the absolute radiance calibration for several instrument modes. This improvement along with the IR files and constants listed in Section 2.1 with effective dates before 2010-01-01 are included in in Version 2 archived in the PDS (McLaughlin, et al., 2014g). Additionally, Version 1 of the HRI-IR Mars EPOCh data was reprocessed during lien resolution with the same set of improvements and archived as Version 1 in the PDS (McLaughlin, et al., 2014h).

2.10.3 EPOCh Earth and Mars VIS Image Data

Version 1 of the HRI-VIS and MRI-VIS Earth and Mars EPOCh data archived with the PDS (McLaughlin, et al., 2009b, McLaughlin, et al., 2009c, McLaughlin, et al., 2010a, and McLaughlin, et al., 2010b) does not include the horizontal stripes removal, improved electronic crosstalk values, and revised absolute radiance calibration constants for several filters. These improvements, most of which are captured in the VIS files and constants listed in Section 2.1 with effective dates before 2010-01-01, are included in Version 2 archived in the PDS

(McLaughlin, et al., 2012d, McLaughlin, et al., 2012e, McLaughlin, et al., 2012f, and McLaughlin, et al., 2012g).

2.11 PDS Version 3

2.11.1 Tempel 1 IR Spectrometer Data

Version 3 of the calibrated HRI-IR Tempel 1 data differ from version 2 for the following items:

- A flat field was derived from lunar observations. This flat field was processed using quadrant based linearization coefficients and takes into account the anti-saturation filter response.

- In late 2010, it was discovered that the IR spectroscopic radiometric calibration curves were in error by a factor of 2. A new calibration curve, valid inside and outside the anti-saturation filter, processed using quadrant based linearization coefficients and corrected by the factor of 2, has been generated and applied to these data.

- Slightly revised time stamps due to a correction to how subsecond clock ticks were computed between Deep Impact and EPOXI pipelines.

2.11.2 Hartley 2 IR Spectrometer Data

Version 3 of the calibrated HRI-IR Hartley 2 data differ from version 2 for the following items:

- Day of year (DOY) 307 is no longer processed with an in scene dark but is instead processed with a manually scaled master dark. The scaling is optimized for each scan. The final radiance product of these data is improved by making this change.

- DOYs 311 through 313 are no longer processed with a scaled master dark but are instead processed with an in scene dark like those observations acquired outside the closest approach time. Because the spacecraft pointing has put the comet nearer to the end of an HRI-IR scan, the second frame of a scan is used for dark subtraction for DOYs 311-313. The final radiance product of these data is improved by making this change.

- All data are processed using an average per scan Optical Bench Temperature (OPTBENT) instead of a frame-by-frame OPTBENT. This temperature is stored into the fits header keyword SMOBENT.

2.11.3 Tempel 1 VIS Images Data

Version 3 of the calibrated Tempel 1 HRI-VIS, MRI-VIS, and ITS-VIS CCD images differ from version 2 for the following items:

- The destriping process was turned on for HRI-VIS and MRI-VIS images, and the pipeline invoked it depending on the scene.

- The application of revised MRI-VIS filter calibration constants.

- Slightly revised time stamps due to a correction to how subsecond clock ticks were computed between Deep Impact and EPOXI pipelines

3. Limitations of the Pipeline

The 2012-2013 version of the EPOXI pipeline used to calibrate the data in the archived PDS datasets listed in Section 1.0 has several limitations that must be taken into account when analyzing the data.

3.1 HRI-IR Instrument

All input calibration elements of the HRI-IR Version 1 pipeline for the Hartley 2 encounter (delivered in June 2011; McLaughlin, et al., 2012a) were based on a quadrant-by-quadrant (i.e., per-quadrant) analysis of the pixel response. With Version 2 (and 3), a pixel-by-pixel (i.e., per-pixel) approach is used in order to better characterize the non-linearity response of the detector, the instrumental dark current background, detector flat field, bad pixel maps, and absolute calibration. In addition, mode dependent master dark frames are created and used for the subset of data where in-scene dark frames are not available. With respect to Version 2, Version 3 implements the following improvement: an average per scan optical bench temperature (SMOBENT) was calculated and used, rather than a frame-by-frame optical bench (OPTBENT) temperature, in all steps of the pipeline that are temperature dependent. During Version 1 processing, we investigated pixel–to-pixel responses and found that the non-linear response function is more accurately reproduced with a pixel-to-pixel derivation (improvement by a factor of 10). Implementing the pixel-by-pixel treatment for linearity in Version 2 (and 3) reduces signal level errors to well below 1% across the scene, removing the gradients observed across the quadrants when treated as a whole. Implementing the average per scan optical bench temperature removed obvious striping in the radiance files along the spatial direction when a spatial scan cube was generated, an effect not obvious when looking at single frames.

The dark frame background level is strongly dependent on the exposure time, temperature of the instrument (bench, electronics, and detector), mode, and the recent history of detector resets and readouts. A careful analysis of the dark level was performed and optimized to correct for these effects with an extensive dark frame set and instrument temperature models. Outside of encounter where the cometary signal was lower (for Hartley 2, encounter is considered to range from November 3-6, 2012, for this purpose), in-scene darks are used without any scaling to estimate the dark signal in an IR frame and the result is good to within ±8 DN across a scan and good to within ±6 DN in frames with cometary signal. Closer to encounter, there are no dark frames to use within a scan and a scaled master dark is used instead. In Version 1, master dark frames were created for all modes from unbinned full frame data, but the master dark wasn't able to reproduce and remove the observed sub-frame structure due to saturated pixels outside of the reset area of the detector, and thus the dark subtraction was not suitable. The Version 2 (and 3) master dark frames are created from dark frames in each mode such that mode dependent structure is retained in the master dark and removed in the dark subtraction step. Also, the scaling of the master dark is optimized for each scan across the scene where the signal is high,

variable and fills the field of view. The resulting data after this dark correction are good to within ±15 DN. While the residual dark level error is not normally an issue in the 2.0-4.5 μm wavelength range where the sensitivity of the detector is high, it becomes more of an issue at short (<2.0 μm) and long (>4.5 μm) wavelengths where the sensitivity of the detector drops rapidly. As a consequence, one should be cautious when interpreting any data below 2.0 μm or above 4.5 μm.

All HRI-IR calibration efforts to date have used OPTBENT or SMOBENT and IRFPAT as encoded in the FITS headers by the calibration pipeline. The project discovered that the long-standing difference of approximately 0.9 K between the calibration pipeline values in the FITS headers and the spacecraft tabulations of the same instrument temperatures are due to a different DN temperature algorithm encoded in the AMMOS spacecraft pipeline. Since all calibration efforts to date have relied on the temperatures in the pipeline, any temperatures used from the tables of spacecraft temperatures archived in Hampton (2007) and Carcich, et al. (2014) should be adjusted downward, i.e., use T_s/c - 0.9K, before using them in any steps of the calibration process. For more detail, see Wellnitz, et al., 2014.

The flat-field correction of HRI-IR data is quite reliable and reproduces the transmission function of the anti-saturation filter quite well. The flat field also corrects for scattered light into the anti-saturation filter region.

We have observed some variation in the locations of bad pixels during flight, both during Deep Impact and EPOXI, and an increase in bad pixels with time. For the Version 2 delivery, we use an extensive set of dark frames acquired in February 2011 to derive the bad pixel maps. The number of bad pixels increased from 1.53% of the active area of the detector in Version 1 of the Hartley 2 data to 1.96% in Version 2. This is due in part to additional criteria imposed during pixel characterization. In addition, there may be some uncharacterized bad pixels that changed throughout the duration of the Hartley 2 data collection. Bad pixels are identified in the image quality/flags extension of the raw and calibrated data and are interpolated over only in the irreversible radiance (RAD) products; bad pixels are still present and are not reclaimed in reversible radiance (RADREV) products.

The absolute and relative spectral sensitivity calibrations are limited to the ~10% level. This uncertainty is even more pronounced below 1.5 μm, where there is higher spectral resolution and therefore any residuals from poor wavelength matching is more pronounced, and above 4.5 μm where reference stellar spectra have low signal and the absolute calibration is not as good. In addition, the effect of the anti-saturation filter introduces uncertainties in the radiometric calibration a long wavelengths, where the filter reduces the signal so that the thermal contribution of the nucleus does not saturate the detector. As a result, the sensitivity of the detector above 4.3 μm in the anti-saturation zone drops very rapidly to zero at 4.6 μm, and one should be cautious when interpreting data in this region.

The HRI-IR exhibits scattered light effects, in addition to those described above in the anti-saturation filter region, that are not corrected in the calibration pipeline. In previous mission phases, response at the 1-2% level was seen 10 pixels off the bright limb of the Moon. And a ghost image at the 3-4% level is seen about 35 slit widths away from the primary image in the cross-slit direction.

Detection and correction of cosmic ray signatures in HRI-IR frames is not yet reliable. Such signatures are best detected by differencing pairs of successive frames. But no pipeline process is currently being applied to detect or correct cosmic rays in individual frames.

Finally, any horizontal striping through some images indicates missing data (pixels), which the pipline identifies in image quality/flags extension of the raw and calibrated. However, missing pixels in a frame of an exposure ID that is used as the in-scene dark frames dark will contaminate the calibrated observations of the same ExpID and will appear as additional horizontal stripes. The pipeline does not identify these contaminated pixels in the image quality/flags extension.

3.2 HRI-VIS and MRI-VIS Instruments

The small amount of geometric distortion in the VIS images is not normally being corrected. Radial distortion is ≤0.1 pixel in the MRI-VIS and likely less for the HRI-VIS (but it has not been measured for HRI-VIS). The two central rows of the CCDs in each camera are 1/6 of a pixel smaller vertically than a normal row. Therefore, reconstructed images, which have uniform row spacing, have a 1/3-pixel extension introduced at the center of the array. Thus for two features on either side of the midpoint line, the vertical component of the *actual* angular separation between those features is one-third of a pixel less than their measured difference in vertical pixels in the image. As for all geometric distortions, correction of this distortion will require resampling of the image and an attendant loss in spatial resolution. The inflight focal length measurements result in pixel IFOVs that are slightly different than the canonical 10 μrad for MRI-VIS and 2 μrad for HRI-VIS. The actual MRI-VIS IFOV is about 0.08% smaller, and the actual HRI-VIS IFOV varies from 0.002% larger to 0.02% smaller, depending on the filter. The relative boresight alignments between the instruments are uncertain to about ±1 MRI-VIS pixel.

The spatial resolution of the MRI-VIS degrades slightly from the center to the edges of the FOV with the PSF width growing by about 50% at the corners of the FOV. The HRI-VIS is out of focus with a PSF FWHM of ~9 pixels; the detailed PSF varies with filter.

Several limitations on the accuracy of the radiometric calibrations exist. The calibration pipeline assumes that the VIS CCD response is perfectly linear. In reality, departures from linearity exist, with the actual response being up to 1% high relative to perfect linearity in the signal range between 100 and 12000 DN and up to 2% low relative to perfect linearity below 100 DN and above 12000 DN. The bias correction in Modes 7 and 8 cannot be derived from serial overclocked (SOC) pixels, since SOCs do not exist in these modes. The fixed bias estimate used in these modes can be off by ±5 DN. The residual horizontal striping that remains after quad-level bias subtraction can range from 1 – 10 DN if left uncorrected. For those cases where the stripe-removal algorithm can be applied, the residual striping is reduced to ~0.2 DN. Frame transfer smear correction is accurate to only about 1 DN.

The uncertainty in conversion to absolute radiometric units is estimated to be 5% for HRI-VIS except for the 950-nm filter, where the uncertainty is ~10%. For MRI-VIS, the uncertainties are about 10% for all but the UV filters, which have an uncertainty of 20%. The actual central wavelength of the MRI-VIS 387-nm filter remains uncertain; it could be up to 2 nm longward of

its nominal value. Several filters have red leaks that may produce non-negligible signal – they include the 350, 550, 650, and 850-nm HRI-VIS filters and the 309-nm MRI-VIS filter.

The quality and uncertainty in the radiometric calibration for each pixel is recorded in the quality and SNR extensions. Analyses that involve photometric precision should refer to those extensions to determine the error bars on their measurements. In addition, flat-field calibrations leave uncorrected pixel-to-pixel variations of ~0.5%. The 1/6-pixel narrower central rows collect only 5/6 of the charge of a normal row. This effect is corrected by the flat-field division so that the pixels in these rows have the correct scene radiance assigned to them. However, point-source or disk-integrated photometric measurements using aperture photometry areas that include these central rows will be slightly distorted unless special adjustments are made (e.g., an extra 1/6-pixel worth of signal is added to the pixels in each of these two rows in the reconstructed images, as described in Appendix A of Belton, et. al., Icarus, 213, 345-368, 2011). The ADC quantization error is ~1 DN (this effect is appears in the SNR map). Data compression, if used, can result in quantization errors that dominate the pixel-level noise (this effect also appears in the SNR map and is explained in Carcich, 2014). Cross talk between CCD quadrants is corrected but may leave residual uncorrected signal of up to 2 DN from a saturated scene area within a quadrant. Internal scattered light can produce measurable diffuse scatter within the FOV. This scatter is normally small enough to be ignored, but should not be neglected when doing high-contrast photometric measurements. The scatter is about 6x worse in the MRI-VIS than in the HRI-VIS, is 5x worse in the IR filters than in typical filters for both cameras, and is about 3x worse in the HRI-VIS violet filter than in the other HRI-VIS filters. In addition, a 6-pronged diffraction spike ray pattern is produced at a level of up to 2×10^{-8}/source pixel. Finally, cosmic ray signatures are not reliably removed, and the VIS destripe process may remove scattered light the reaches the edges of an image for a bright source such as Earth (section 2.4 explains how to back out this reversible step or 'restripe' the image).

4. References

Carcich, B., D. Hampton, and S. McLaughlin, 2014, EPOXI HRII/HRIV/MRI Instrument Temperatures V3.0, DIF-CAL-HRII/HRIV/MRI-6-EPOXI-TEMPS-V3.0, NASA Planetary Data System.

Carcich, B., 2014, Deep Impact/EPOXI: Explanation of Quantized Signal-to-Noise in VIS CCD Images, archived in Deep Impact /EPOXI Documentation Set V4.0, DI-C-HRII/HRIV/MRI/ITS-6-DOC-SET-V4.0, NASA Planetary Data System, 2014.

Hampton, D., 2007, Deep Impact HRII/HRIV/MRI Instrument Temperatures V1.0, DIF-C-HRII/HRIV/MRI-6-TEMPS-V1.0, NASA Planetary Data System.

Klaasen, K.P., M.F. A'Hearn, M. Baca, A. Delamere, M. Desnoyer, T. Farnham, O. Groussin, D. Hampton, S. Ipatov, J. Li, C. Lisse, N. Mastrodemos, S. McLaughlin, J. Sunshine, P. Thomas, and D. Wellnitz, 2008, Deep Impact Instrument Calibration, Rev. Sci. Instrum., 79, 091301, doi:10.1063/1.2972112.

Klaasen, K.P., M. A'Hearn, S. Besse, D. Bodewits, B. Carcich, T. Farnham, L. Feaga, O. Groussin, D. Hampton, M. Huisjen, M.S. Kelley, S. McLaughlin, F. Merlin, S. Protopapa, J.

Sunshine, P. Thomas, and D. Wellnitz, 2013, EPOXI Instrument Calibration, Icarus, 225(1), 643–680, doi:10.1016/j.icarus.2013.03.024.

McLaughlin, S.A., B. Carcich, S.E. Sackett, and K.P. Klaasen, 2012a, EPOXI Hartley2 Encounter - HRII Calibrated Spectra V1.0, DIF-C-HRII-3/4-EPOXI-HARTLEY2-V1.0, NASA Planetary Data System.

McLaughlin, S.A., B. Carcich, S.E. Sackett, and K.P. Klaasen, 2013a, EPOXI 103P/Hartley2 Encounter - HRII Calibrated Spectra V2.0, DIF-C-HRII-3/4-EPOXI-HARTLEY2-V2.0, NASA Planetary Data System.

McLaughlin, S.A., B. Carcich, S.E. Sackett, K.P. Klaasen, L.M. Feaga, and S. Protopapa, 2014a, EPOXI 103P/Hartley2 Encounter - HRII Calibrated Spectra V3.0, DIF-C-HRII-3/4-EPOXI-HARTLEY2-V3.0, NASA Planetary Data System.

McLaughlin, S.A., B. Carcich, S.E. Sackett, and K.P. Klaasen, 2012b, EPOXI 103P/ Hartley2 Encounter - HRIV Calibrated Images V1.0, DIF-C-HRIV-3/4-EPOXI-HARTLEY2-V1.0, NASA Planetary Data System.

McLaughlin, S.A., B. Carcich, S.E. Sackett, and K.P. Klaasen, 2012c, EPOXI 103P/ Hartley2 Encounter - MRI Calibrated Images V1.0, DIF-C-MRI-3/4-EPOXI-HARTLEY2-V1.0, NASA Planetary Data System.

McLaughlin, S.A., B. Carcich, D. Deming, K.P. Klaasen, and D.D. Wellnitz, 2009a, EPOXI Earth Obs - HRII Calibrated Spectra V1.0, DIF-E-HRII-3/4-EPOXI-EARTH-V1.0, NASA Planetary Data System.

McLaughlin, S.A., B. Carcich, D. Deming, T. Livengood, T. Hewagama, K.P. Klaasen, and D.D. Wellnitz, 2014g, EPOXI Earth Obs - HRII Calibrated Spectra V2.0, DIF-E-HRII-3/4-EPOXI-EARTH -V2.0, NASA Planetary Data System.

McLaughlin, S.A., B. Carcich, D. Deming, K.P. Klaasen, and D.D. Wellnitz, 2009b, EPOXI Earth Obs - HRIV Calibrated Images V1.0, DIF-E-HRIV-3/4-EPOXI-EARTH-V1.0, NASA Planetary Data System.

McLaughlin, S.A., B. Carcich, D. Deming, T. Livengood, T. Hewagama, K.P. Klaasen, and D.D. Wellnitz, 2012d, EPOXI Earth Obs - HRIV Calibrated Images V2.0, DIF-E-HRIV-3/4-EPOXI-EARTH -V2.0, NASA Planetary Data System.

McLaughlin, S.A., B. Carcich, D. Deming, K.P. Klaasen, and D.D. Wellnitz, 2009c, EPOXI Earth Obs - MRI Calibrated Images V1.0, DIF-E-MRI-3/4-EPOXI-EARTH-V1.0, NASA Planetary Data System.

McLaughlin, S.A., B. Carcich, D. Deming, T. Livengood, T. Hewagama, K.P. Klaasen, and D.D. Wellnitz, 2012e, EPOXI Earth Obs - MRI Calibrated Images V2.0, DIF-E-MRI-3/4-EPOXI-EARTH-V2.0, NASA Planetary Data System.

McLaughlin, S.A., B. Carcich, D. Deming, T. Livengood, T. Hewagama, K.P. Klaasen, and D.D. Wellnitz, 2014h, EPOXI Mars Obs - HRII Calibrated Spectra V1.0, DIF-E-HRII-3/4-EPOXI-MARS –V1.0, NASA Planetary Data System.

McLaughlin, S.A., B. Carcich, D. Deming, T. Livengood, K.P. Klaasen, and D.D. Wellnitz, 2010a, EPOXI Mars Obs - HRIV Calibrated Images V1.0, DIF-M-HRIV-3/4-EPOXI-MARS-V1.0, NASA Planetary Data System.

McLaughlin, S.A., B. Carcich, D. Deming, T. Livengood, T. Hewagama, K.P. Klaasen, and D.D. Wellnitz, 2012f, EPOXI Mars Obs - HRIV Calibrated Images V2.0, DIF-M-HRIV-3/4-EPOXI-MARS-V2.0, NASA Planetary Data System.

McLaughlin, S.A., B. Carcich, D. Deming, T. Livengood, K.P. Klaasen, and D.D. Wellnitz, 2010b, EPOXI Mars Obs - MRI Calibrated Images V1.0, DIF-M-MRI-3/4-EPOXI-MARS-V1.0, NASA Planetary Data System.

McLaughlin, S.A., B. Carcich, D. Deming, T. Livengood, T. Hewagama, K.P. Klaasen, and D.D. Wellnitz, 2012g, EPOXI Mars Obs - MRI Calibrated Images V2.0, DIF-M-MRI-3/4-EPOXI-MARS-V2.0, NASA Planetary Data System.

McLaughlin, S.A., B. Carcich, S.E. Sackett, K.P. Klaasen, and L. Feaga, 2014i, EPOXI C/Garradd (2009 P1) - HRII Calibrated Spectra V1.0, DIF-C-HRII-3/4-EPOXI-GARRADD-V1.0, NASA Planetary Data System.

McLaughlin, S.A., B. Carcich, S.E. Sackett, K.P. Klaasen, and T. Farnham, 2014j, EPOXI C/Garradd (2009 P1) - HRIV Calibrated Images V1.0, DIF-C-HRIV-3/4-EPOXI-GARRADD-V1.0, NASA Planetary Data System.

McLaughlin, S.A., B. Carcich, S.E. Sackett, K.P. Klaasen, and T. Farnham, 2014k, EPOXI C/Garradd (2009 P1) - MRI Calibrated Images V1.0, DIF-C-MRI-3/4-EPOXI-GARRADD-V1.0, NASA Planetary Data System.

McLaughlin, S.A., B. Carcich, S.E. Sackett, K.P. Klaasen, and L. Feaga, 2014l, EPOXI C/ISON (2012 S1) - HRII Calibrated Spectra V1.0, DIF-C-HRII-3/4-EPOXI-ISON-V1.0, NASA Planetary Data System.

McLaughlin, S.A., B. Carcich, S.E. Sackett, K.P. Klaasen, and T. Farnham, 2014m, EPOXI C/ISON (2012 S1) - MRI Calibrated Images V1.0, DIF-C-MRI-3/4-EPOXI-ISON-V1.0, NASA Planetary Data System.

McLaughlin, S.A., B. Carcich, S.E. Sackett, K.P. Klaasen, L. Feaga, and S. Protopapa, 2014b, EPOXI Inflight Lunar Cals - HRII Calibrated Spectra V1.0, DIF-L-HRII-3/4-EPOXI-LUNAR-CALS-V1.0, NASA Planetary Data System.

McLaughlin, S.A., B. Carcich, T. McCarthy, M. Desnoyer, K.P. Klaasen, L. Feaga, and S. Protopapa, 2014c, Deep Impact 9P/Tempel Encounter - Reduced HRII Spectra V3.0, DIF-C-HRII-3/4-9P-ENCOUNTER-V3.0, NASA Planetary Data System.

McLaughlin, S.A., B. Carcich, T. McCarthy, M. Desnoyer, K.P. Klaasen, and D.D. Wellnitz, 2014d, Deep Impact 9P/Tempel Encounter - Reduced HRIV Images V3.0, DIF-C-HRIV-3/4-9P-ENCOUNTER-V3.0, NASA Planetary Data System.

McLaughlin, S.A., B. Carcich, T. McCarthy, M. Desnoyer, K.P. Klaasen, and D.D. Wellnitz, 2014e, Deep Impact 9P/Tempel Encounter - Reduced MRI Images V3.0, DIF-C-MRI-3/4-9P-ENCOUNTER-V3.0, NASA Planetary Data System.

McLaughlin, S.A., B. Carcich, T. McCarthy, M. Desnoyer, K.P. Klaasen, and D.D. Wellnitz, 2014f, Deep Impact 9P/Tempel Encounter - Reduced ITS Images V3.0, DII-C-ITS-3/4-9P-ENCOUNTER-V3.0, NASA Planetary Data System.

Wellnitz, D.D, M.F. A'Hearn, B. Carcich, L. Feaga, and S. Protopapa, 2014, Deep Impact/EPOXI: Influences of the IR Temperature Measurements on the Calibration Pipeline, archived in Deep Impact /EPOXI Documentation Set V4.0, DI-C-HRII/HRIV/MRI/ITS-6-DOC-SET-V4.0, NASA Planetary Data System, 2014.